

NUMERICAL ANALYSIS OF GENERALIZED AERODYNAMIC FORCES CONSIDERING LAMINAR-TURBULENT TRANSITION ON A NLF WING

Carlos Sebastia Saez¹, Jaime Martin Ferres¹ & Mirko Hornung¹

¹Technical University of Munich, Chair of Aircraft Design, Boltzmannstr. 15, 85748 Garching b. München

Abstract

The wing's dynamic aeroelastic stability analysis, referred to as flutter analysis, typically involves potential-flow-theory-based methods to model unsteady aerodynamics, which do not consider viscous or non-linear effects. Modern sailplane wings with Natural-Laminar-Flow (NLF) airfoils present significant chord-wise runs of laminar boundary layers. Assuming an inviscid or completely turbulent flow over the wing chord could result in completely wrong predictions of the unsteady aerodynamic characteristics of the wing and, hence, an inaccurate prediction of the dynamic aeroelastic behavior. This study presents a coupled Finite Element beam model of a sailplane with a Computational Fluid Dynamics model to calculate the Generalized Aerodynamic Forces (GAF). The aeroelastic behavior is investigated by means of aerodynamic damping and stiffness. The influence of transition on the unsteady aerodynamic response of a modern sailplane's NLF wing is investigated numerically with the Gamma-Transition Model for a range of Re-numbers and reduced frequencies k_{red} . The GAF entries are compared to the results obtained with the fully turbulent Spalart-Allmaras (SA) model. This investigation underscores the significance of modeling transition in predicting the aerodynamic performance for NLF wings to account for viscous effects and mitigate uncertainties associated with flutter prediction.

Keywords: Aeroelasticity, CFD, Generalized Aerodynamic Forces, Loose Coupling

1. Introduction

The dynamic aeroelastic stability analysis of an aircraft involves the study of the interaction between aerodynamic, elastic and inertial loads, potentially leading to self-excited oscillations. Typically, unsteady aerodynamic loads are calculated using potential-based approaches such as the Doublet Lattice Method (DLM), which is widely recognized as a state-of-the-art tool for flutter prediction [4, 5]. However, potential-based methods do not consider viscous or non-linear effects. The more relevant the viscous effects and the nonlinear characteristics of the aerodynamic system the higher these uncertainties. To mitigate uncertainties and rectify the aerodynamic behavior predicted by lower fidelity methods, higher fidelity models or wind tunnel experiments may be introduced [12].

Modern sailplane wings with NLF airfoils present an almost gradient-free pressure side and under free-flight Re-numbers the boundary layer remains laminar beyond the flap hinge. To prevent the formation of laminar separation bubbles (LSB) and the resulting increase in drag, a turbulator is strategically placed just upstream of the main pressure rise. However, a structural deformation in form of a change in effective angle of attack can cause a sudden shift of the boundary layer transition towards the leading edge. This may impact the unsteady aerodynamic response, which is not accounted for in the classic flutter prediction.

In the scope of this study, CFD is used to predict the time-accurate aerodynamic behavior of a sailplane's high aspect ratio NLF wing under unsteady conditions. To analyze the impact of an unsteady boundary layer transition, the CFD simulations are performed with the Gamma-Transition model. The results are compared to the fully turbulent Spallart-Allmaras (SA) model to asses the relevance of the viscous effects related to transition. The unsteady boundary conditions for the CFD simulations are defined based on the results from a modal analysis performed with a FE beam model of the sailplane structure in MSC-Nastran. The FE solution is coupled with the CFD solver by means of imported eigenvectors and eigenfrequencies to obtain the Generalized Aerodynamic Forces (GAF),

which can later be directly used to perform a flutter calculation or to correct the GAF matrix obtained with lower fidelity methods [10].

The unsteady aerodynamic response to defined inputs, here structural displacements, is analyzed in terms of nonlinear phenomena. These non-linearities may be a result of a structural deformation amplitudes outside the linear limits or due to the wide range of different reference flow conditions, e.g. variable free-stream flow velocity [6, 7, 11]. In [8], it was demonstrated that at specific combinations of angle of attack and Re-number, the aerodynamic characteristics exhibit non-linearites due to an unsteady transition caused by periodic flap oscillations and the consequent viscous effects in the boundary layer.

2. Theory and Numerical Methods

The following section presents the theoretical background for the aeroelastic analysis including the coupling between the FEM and CFD to obtain the GAF matrix.

2.1 Aeroelastic Equations

The basis for the aeroelastic analysis is the system of equations coupling inertial, elastic and aero-dynamic loads:

$$\mathbf{M}\ddot{\mathbf{x}} + \mathbf{D}\dot{\mathbf{x}} + \mathbf{K}\mathbf{x} = \mathbf{f},\tag{1}$$

where M is the mass matrix, D is the damping matrix, K the stiffness matrix and f represents the external forces. The external forces include aerodynamic forces that can be divided in pressure $f_{p,i}$ and friction $f_{f,i}$ forces acting on each surface element i:

$$\mathbf{f_{p,i}} = c_{p,i} \, d\mathbf{S_i} \tag{2}$$

$$\mathbf{f_{f,i}} = \mathbf{c_{f,i}} \, dS_i \tag{3}$$

where $d\mathbf{S_i}$ is the surface vector for a surface element i and dS_i is its magnitude. The coefficients $c_{p,i}$ and $\mathbf{c_{f,i}}$ represent the pressure coefficient and the friction coefficient, both normalized with dynamic pressure q_{∞} .

The system of equations can be transformed from physical coordinates $\mathbf{x}(t)$ to modal or generalized coordinates $\mathbf{q}(t)$ for a more convenient and efficient representation. The modal coordinates or eigenvectors are obtained by means of a modal analysis and in this context a purely harmonic assumption is applied:

$$\mathbf{x}(t) = \mathbf{x_0} \, e^{i\omega t} \tag{4}$$

Solving the eigenvalue problem delivers the eigenvectors ϕ and the eigenvalues λ of the system. The eigenfrequency ω can then be calculated from the eigenvalues as $\omega_i = \sqrt{\lambda_i}$. The modal matrix $\phi = [\phi_1, \phi_2, ..., \phi_N]$ contains N mode shapes, arranged according to the corresponding eigenvalue, where $\lambda_1 \leq \lambda_2 \leq ... \leq \lambda_N$. The displacement vector $\mathbf{x}(t)$ can then be expressed as:

$$\mathbf{x}(t) = \phi \mathbf{q}(t) \tag{5}$$

The generalized matrices are obtained analogously:

$$\mathbf{M_{gen}} = \phi^T \mathbf{M} \phi, \quad \mathbf{D_{gen}} = \phi^T \mathbf{D} \phi, \quad \mathbf{K_{gen}} = \phi^T \mathbf{K} \phi \quad \text{and} \quad \mathbf{f_{gen}} = \phi^T \mathbf{f},$$
 (6)

and equation 1 can be expressed in generalized form:

$$\mathbf{M}_{\mathbf{gen}}\ddot{\mathbf{q}}(t) + \mathbf{D}_{\mathbf{gen}}\dot{\mathbf{q}}(t) + \mathbf{K}_{\mathbf{gen}}\mathbf{q}(t) = q_{\infty}\mathbf{f}_{\mathbf{gen}}(t). \tag{7}$$

Each element of the matrix \mathbf{f}_{gen} represents the aerodynamic response to a structural deformation in eigenmode n and generalized with mode m. Each $f_{gen,mn}$ entry is the result of the summation of all N_{CFD} generalized force components $f_{gen,mn,i}$ acting on each wing surface cell i. The expression can be seen in equation 8.

$$f_{gen,mn} = \sum_{i=1}^{N_{CFD}} f_{gen,mn,i} \tag{8}$$

The component of $f_{gen,mn,i}$ resulting from pressure forces $f_{gen,mn,p,i}$ is determined as:

$$f_{gen,mn,p,i} = c_{p,n,i} \phi_{m,i} d\mathbf{S}_n, i \tag{9}$$

Alternatively, $f_{gen,mn,p}$ can be expressed as an integration over the entire surface:

$$f_{gen,mn,p} = \int_{S} c_{p,n} \, \phi_{m,i} \, d\mathbf{S}_n \tag{10}$$

The same procedure can be followed to account for friction loads $f_{gen,mn,f}$.

The time dependent unsteady aerodynamic loads are obtained in CFD in the time-domain and they can be transformed into the frequency space to solve the complex eigenvalue problem in the flutter analysis:

$$\left[\mathbf{M}_{\mathbf{gen}}s^2 + \mathbf{D}_{\mathbf{gen}}s + \mathbf{K}_{\mathbf{gen}} - q_{\infty}\mathbf{f}_{\mathbf{gen}}\right]u = 0,$$
(11)

where s is the Laplace variable and u the modal displacement.

The Laplace variable can further be substituted by the dimensionless complex eigenvalue p:

$$p = \frac{l_{ref}}{U_{\infty}}s,\tag{12}$$

with its imaginary part being the reduced frequency k_{red} and its real component the reduced damping g. The reduced frequency can also be written as:

$$k_{red} = \frac{\omega l_{ref}}{U_{m}},\tag{13}$$

where ω is the angular frequency, l_{ref} is the reference length, which is half the mean aerodynamic chord and U_{∞} is the reference air speed.

By combining equation 11 and 12, and dividing the GAF entries into their real and imaginary components, one obtains the following complex eigenvalue problem:

$$\left[\frac{U_{ref}^{2}}{l_{ref}^{2}}\mathbf{M_{gen}}p^{2} + \frac{U_{\infty}}{l_{ref}}\left(\mathbf{D_{gen}} - \frac{1}{2}\frac{\rho l_{ref}U_{\infty}}{k_{red}}Im(\mathbf{GAF}(k_{red}))\right)p + \left(\mathbf{K_{gen}} - q_{\infty}Re(\mathbf{GAF}(k_{red}))\right)\right]u = 0.$$
(14)

Each entry GAF_{mn} of the complex GAF matrix represents the contribution in terms of magnitude and phase shift of the aerodynamic force vector resulting from a displacement in mode n and generalized with mode m. Hence, the GAF matrix establishes the connection between the aerodynamic and the structural dynamic model. In equation 14, the imaginary part of GAF can be interpreted as aerodynamic damping, while the real part can be interpreted as aerodynamic stiffness.

In the context of flutter analysis, a linear relation between the structural deformation and the unsteady aerodynamic response is assumed [1], which leads to small perturbations around a reference state and boundary conditions at which non-linearities like flow separations or pronounced shock motions may not occur [11]. A case study regarding the amplitude of the structural deformation and flow conditions is needed to ensure a linear relation between input displacement and aerodynamic response. Furthermore, linear potential theory based methods, like DLM, are state-of-the-art tools to compute the GAF matrix. Each aerodynamic force component due to a modal deformation in eigenmode n and generalized with mode m does only contain one single complex element, thus neglecting higher harmonic components that may appear due to non linear effects.

3. Model Description and Numerical Setup

The investigated geometry corresponds to the NLF high aspect ratio wing of the high-performance sailplane Ventus 3 designed by the sailplane manufacturer Schempp-Hirth Flugzeugbau GmbH. The wing consists of five span-wise distributed NLF profiles -excluding the winglet. In the scope of this study, only the b/2=9m semi-span wing is modeled, which is extended to the symmetry plane. The mean aerodynamic chord is MAC=0.635m.

3.1 CFD Model

A 3D-unstructured mesh is used for the numerical simulations. Polygon elements are used in the farfield and the boundary layer is resolved with a prism layer with a dimensionless wall distance of y+<1 and a stretch factor of 1.1. Given the need for numerous computational-intensive simulations, the grid refinement is chosen to balance solution accuracy with acceptable computational effort. A mesh with approximately 37 million cells was chosen for all simulations, which also provided a mesh independent solution. The wing's surface mesh can be seen in figure 1.

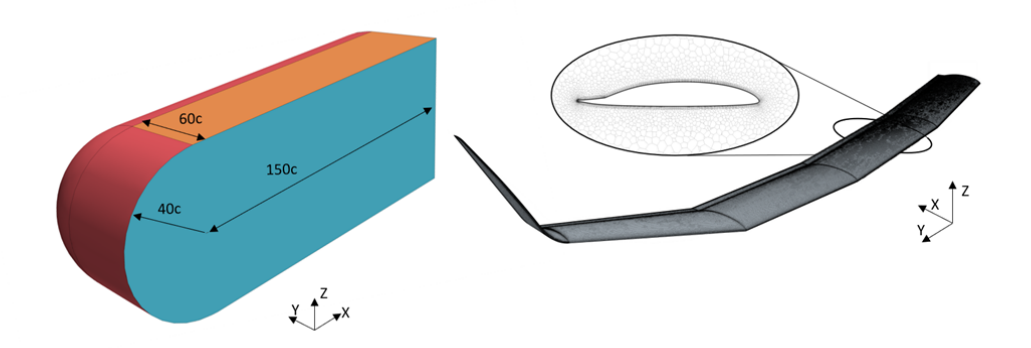


Figure 1 – Left: computational domain and boundary conditions, with *blue*: symmetry plane, *red*: velocity inlet and *orange*: pressure outlet; and right: wing surface mesh with a section detail

Figure 1 presents the computational domain and the boundary conditions used for the simulation. The upper and lower boundaries are set to velocity inlet or pressure outlet depending on the angle of attack α .

The CFD simulations are performed in the commercial software StarCCM+ with the turbulence models SA and Gamma-Transition model, which is coupled with the $k-\omega$ SST model. The Gamma model includes an additional transport equation for the intermittency to predict the onset of transition between a laminar and a turbulent boundary layer. The intermittency formulation is based on experimental data and the production term can be calibrated depending on turbulence intensity and pressure gradients to achieve the desired onset of transition [3]. The transition model parameters are modified based on the calibration suggested by [14].

A segregated solver is used in both cases to couple pressure and velocity and constant density flow is assumed due to the low Mach-numbers (Ma < 0.3). In the Gamma-model setup, a field of turbulent kinetic energy is prescribed upstream of the airfoil to maintain the desired Tu-level of Tu = 0.03% in the far field. Furthermore, a turbulator is modeled as a source of turbulent kinetic energy on the pressure side of the control surface at x/c = 0.91 to force transition and prevent downstream flow separation.

All simulations are performed at $\alpha=2^{\circ}$ and at mean sea level conditions. At this angle of attack, the transition on the pressure side is forced by the turbulator under steady conditions for Re < 5.5e6, which is approximately the maximum Re-number investigated in this study. The selected angle of attack is chosen to prevent non-linearities arising from flow boundary conditions.

A second set of simulations is performed at $\alpha=0^\circ$ and Re=2e6 to asses possible non-linearities arising from flow boundary conditions. At this flow conditions, a small reduction in α may suffice to suddenly shift transition towards the leading edge, causing a rapid change in the boundary layer conditions and inducing viscous effects that cannot be modelled with a fully turbulent model or potential theory based methods.

3.2 Coupling between FEM and CFD

For the computation of the motion induced unsteady aerodynamics, the CFD model mesh is deformed based on the structural mode shapes resulting from a modal analysis of the complete aircraft. A loose coupling between the FEM and CFD is used for this purpose. No feedback from the CFD solution is provided to the FEM model.

First, a modal analysis of the entire sailplane is performed in MSC-Nastran using solution sequence SOL103. The FEM consists of a beam model as shown in figure 2. The results of the modal analysis, i.e. eigenvectors and eigenfrequencies, are imported in StarCCM+. The eigenvectors at each structural node of the FEM are mapped to the CFD wing surface mesh and scaled to obtain a maximal amplitude that still fulfills the boundaries of linear aeroelasticity. All amplitudes are scaled by a factor 0.005, so that the overall maximum displacement amplitude is approximately 1% of the MAC [2].

The unsteady CFD simulations are performed in time-domain. The imported mode displacements are converted to a sinusoidal harmonic oscillation with the corresponding eigenfrequency. A point set is generated with the location of the FEM wing nodes, which is updated at each time step. The CFD mesh is morphed using a B-spline interpolation based on the updated point set.

Pressure and friction force vectors are obtained for each cell on the wing surface with equations 2 and 3. The generalized force vector component in the time-domain acting on each mesh cell i on the wing surface is obtained with equation 9 for a mode m. All generalized force vector components for all wing surface cells N_{CFD} are added to obtain a resultant integral generalized force vector component:

$$f_{gen,mn}(t) = \sum_{i=1}^{N_{CFD}} \mathbf{C}_{n,i}(t)\phi_{m,i},$$
 (15)

where $C_i(t)$ is the sum of pressure and friction forces normalized with q_{∞} . A Fourier transformation is performed to obtain the generalized forces in the frequency-domain. This procedure is repeated for each mode of interest.

A detailed dynamic aeroelastic analysis has to cover a range of structural eigenmodes and associated eigenfrequencies, free-stream conditions, etc. However, the computational effort for such a big design space in CFD is a limiting factor and in the scope of this study, only a couple of eigenmodes and reduced frequencies are investigated. The eigenmodes involving primarily the wing and its deformation are selected for this study. The chosen eigenmodes are shown in figure 2, where displacements are normalized and amplified for visualization purposes.

The reduced frequencies are determined based on the eigenfrequencies f_0 of the corresponding modes by varying the free-stream velocity according to equation 13. The upper velocity limit is defined at $U_{\infty} = 125 \ m/s$ and thus the lowest k_{red} is limited as shown in table 1:

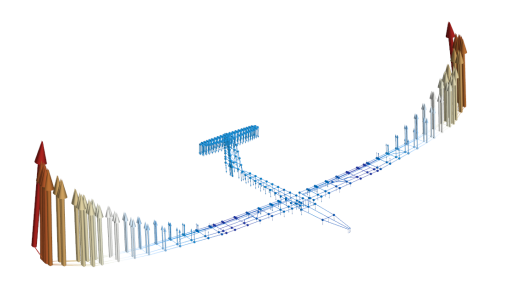
Table 1 – Set of investigated reduced frequencies k_{red} and free-stream flow velocities U_{∞} for the selected structural elastic eigenmodes and corresponding eigenfrequencies.

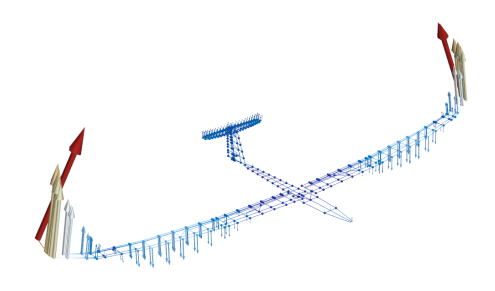
S1, $f_0 = 2.35 \text{ Hz}$				
k_{red}	0.1	0.3		
$U_{\infty}\left[extsf{m/s} ight]$	46.46	15.49		

S2, $f_0 = 7.43 \text{ Hz}$				
k_{red}	0.3	0.6		
$U_{\infty}\left[extsf{m/s} ight]$	49.48	24.74		

S3, $f_0 = 15.22 \text{ Hz}$				
k_{red}	0.3	0.6		
$U_{\infty}\left[extsf{m/s} ight]$	101.31	50.66		

ST, $f_0 = 37.44 \text{ Hz}$				
k_{red}	0.6	0.9		
U_{∞} [m/s]	124.59	83.06		





- (a) Mode 7: 1st symmetric wing bending (S1), f = 2.35 Hz
- (b) Mode 11: 2nd symmetric wing bending (S2), $f = 7.43~{\rm Hz}$





- (c) Mode 17: 3rd symmetric wing bending (S3), f = 15.22 Hz
- (d) Mode 27: 1st symmetric wing torsion (ST), f = 37.44 Hz

Figure 2 – Selected structural elastic eigenmodes.

4. Results

In this section, the results obtained with the fully-turbulent SA model and the Gamma-Transition are presented and compared to assess the impact of an unsteady transition on the unsteady aerodynamic response. The generalized aerodynamic forces obtained with both models are presented and analyzed.

4.1 Flow Analysis and Comparison between SA and Gamma-Transition Model

The flow over the wing has a neglectable cross-flow component in span-wise direction over almost the entire wing surface and the flow can be assumed to have a predominantly 2D character, see figure 3.

Figure 4 depicts the friction coefficients predicted by the SA model and the Gamma-Transition model. The transition model predicts lower friction coefficients compared to a fully turbulent model. This behavior is to be expected as the SA model assumes a completely turbulent boundary layer over the entire surface of the wing, which exhibits a lower du/dy velocity gradient normal to the wing surface than a laminar boundary layer and, thus, higher wall shear stress.

The Gamma model successfully captures the transition between the laminar and the turbulent boundary layer, which can be recognized by the sudden increase in c_f . On the suction side, transition is located at approximately x/c=0.65, and on the pressure side, transition is forced by the turbulator at x/c=0.91. These values are in agreement with the results presented in [8].

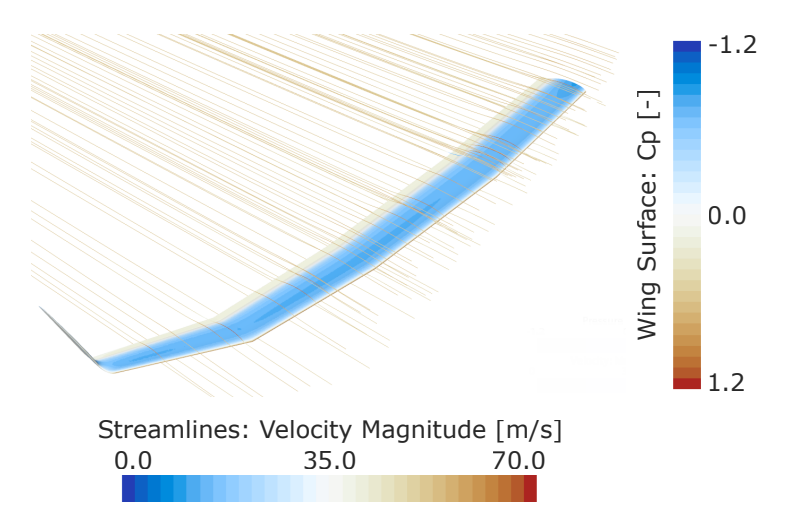


Figure 3 – Streamlines and C_p distribution for S3 case and $k_{red} = 0.6$ computed with SA.

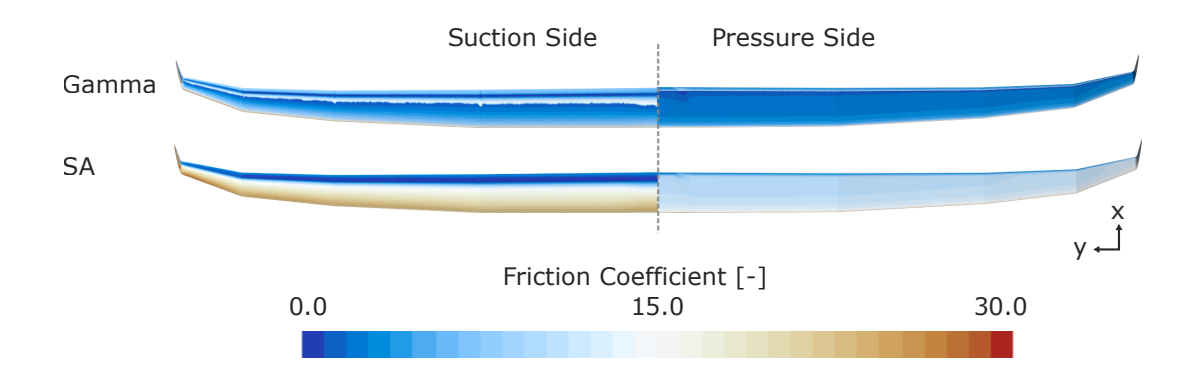


Figure 4 – Friction coefficient distribution on suction and pressure side as predicted with the Gamma-Transition model and the SA turbulence model.

4.2 Generalized Aerodynamic Forces in the Time Domain

Figure 5 shows the generalized aerodynamic forces due to a modal deformation in eigenmode n and generalized with mode m over the normalized harmonic deflection in the time-domain. The generalized forces in the Lissajous figures are normalized with q_{∞} .

The Lissajous figures for a specific GAF entry predicted with both turbulence models display a vertical offset between each other. However, they exhibit a very similar shape and inclination. Thus, the main difference in the aerodynamic response arises from the zero frequency (DC) component. The non-zero Fourier coefficients show similar values, see figure 7.

The shape of the Lissajous figure, i.e. the size of the semi-minor axis of the ellipsis, depends on the modes involved and k_{red} . In case of the bending modes, the GAF entries corresponding to an aerodynamic response in mode n and generalized with the same mode exhibit an elliptical behavior. However, if generalized with another bending mode the size of the semi-minor axis decreases drastically, indicating low modal participation. The semi-minor axes for the GAF entries GAF 27-n consistently show larger magnitudes except for GAF 17-7, indicating a higher modal participation.

The structural deformation in mode n can be correlated with a variation in the effective angle of attack that results from the wing motion. In the case of the first bending mode S1, the dominating eigenvector component is the z-component. During the downward movement, the wing perceives a relative free-stream velocity vector with an upward component resulting in an increase of the effective angle of attack. The relative velocity is highest when the wing crosses the mean position or jig shape and decreases when approaching the maximal deflection.

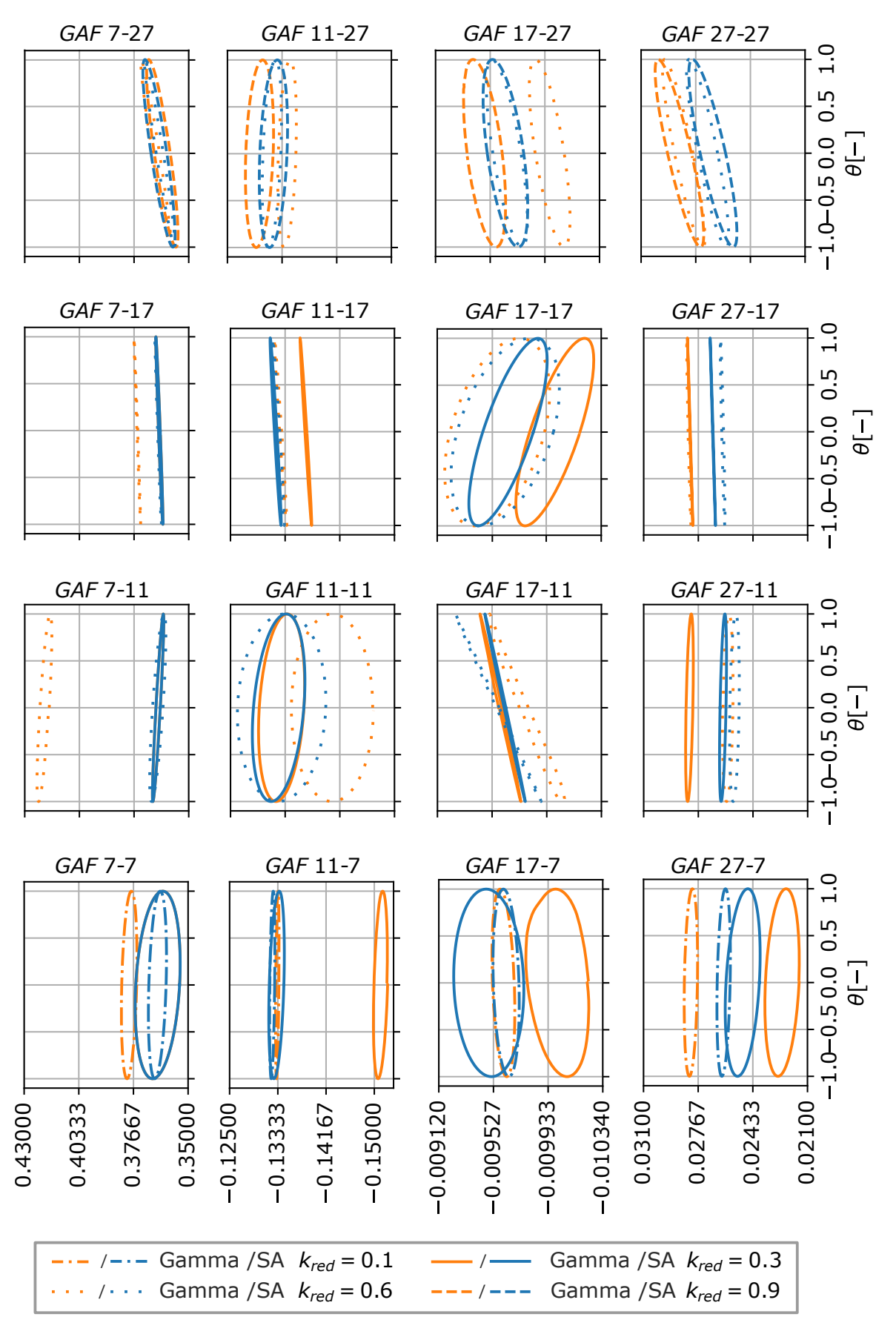


Figure 5 – Lissajous figures of generalized aerodynamic forces GAF_{mn} with n= 7, 11, 17 and 27 over the normalized structural deflection

At a constant oscillating frequency, the higher the magnitude of the eigenvector, the higher the aerodynamic response. As a consequence of the overall lower eigenvectors' magnitude of higher order bending modes and the direction of the structural deformation, the change in magnitude of the oscillating relative free-stream velocity vector decreases. Consequently, the magnitude of the aerodynamic response on a global scale decreases as well. For this reason, the size of the semi-minor axis decreases for bending modes generalized with themselves (GAF 7-7, GAF 11-11 and GAF 17-17) as the order of the bending mode increases. Furthermore, for a specific mode n with a fix eigenfrequency f_0 , the higher k_{red} , the lower is the inflow velocity and thus the larger is the change in effective angle of attack due to a structural deformation. This dependency is depicted in figure 6. Consequently, the semi-minor axis of the Lissajous figures for each GAF entry increases with increasing k_{red} .

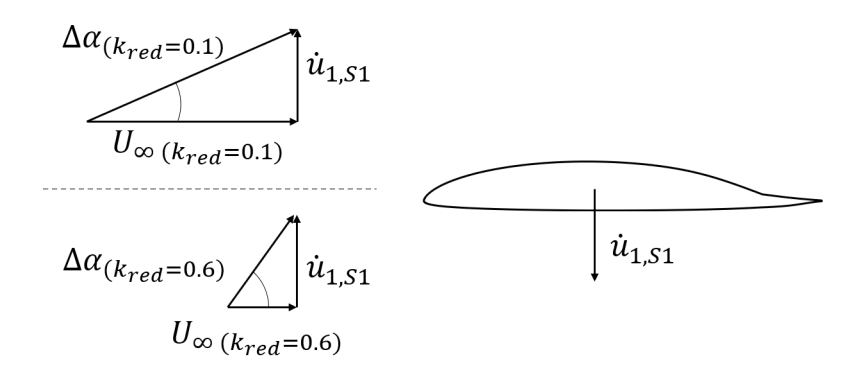


Figure 6 – Variation of effective angle of attack as a function of the reduced frequency k_{red}

As presented in section 2, the generalized forces result from the multiplication of the aerodynamic force vector with an eigenvector ϕ_m , i.e. each force component is scaled with the corresponding eigenvector component of mode m. Generalizing with a mode m that exhibits small eigenvector magnitudes, would scale down the aerodynamic response and result in a lower generalized force. Another influencing factor on the GAF's magnitude is the phase shift between the involved modes. The phase manifests itself in the form of the eigenvectors direction. If the eigenvectors of two different modes at one specific location point in opposite directions, the phase shift is 180° . Higher-order bending modes have eigenvectors of lower magnitude, that, depending on the span-wise location, point in opposite z-directions, see figure 2. Generalizing the aerodynamic force of mode n=7 with modes m=11 or 17 results in smaller generalized forces, see figures 5 and 7.

4.3 Generalized Aerodynamic Forces in the Frequency Domain

To analyze the magnitude of the GAF components more accurately, the GAFs are transformed from the time-domain to the frequency-domain via Fourier transformation. Figures 7 and 8 show the magnitude of the GAF components at different reduced frequencies. The two largest Fourier coefficients are included in this analysis to assess the relevance of higher frequency responses in the dynamic aeroelastic stability problem analysis. As only the oscillating part is of interest, the DC component of the aerodynamic response is neglected in further analysis.

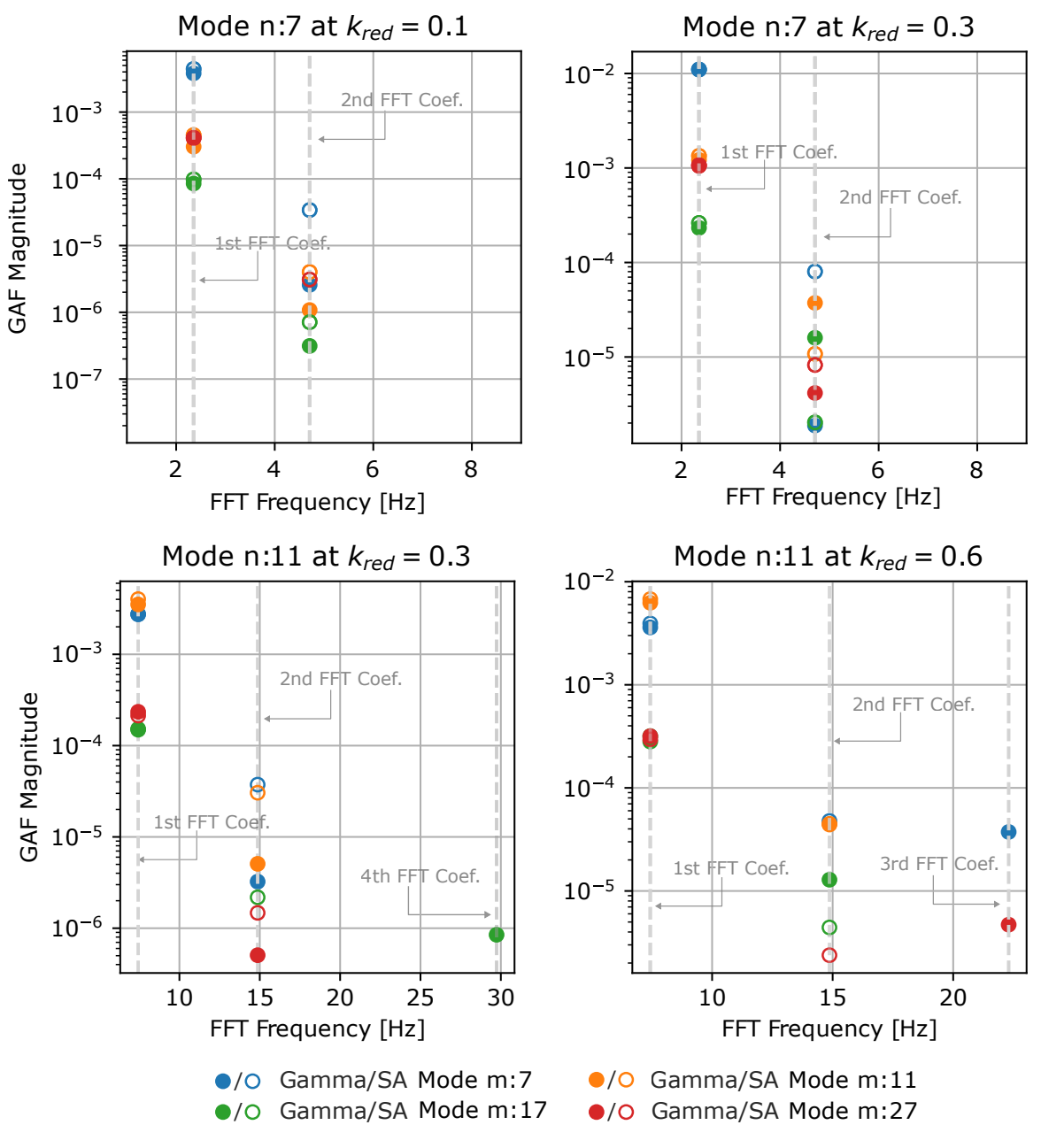


Figure 7 – Magnitude of the GAF entries in the frequency-domain over frequency- continues in figure 8.

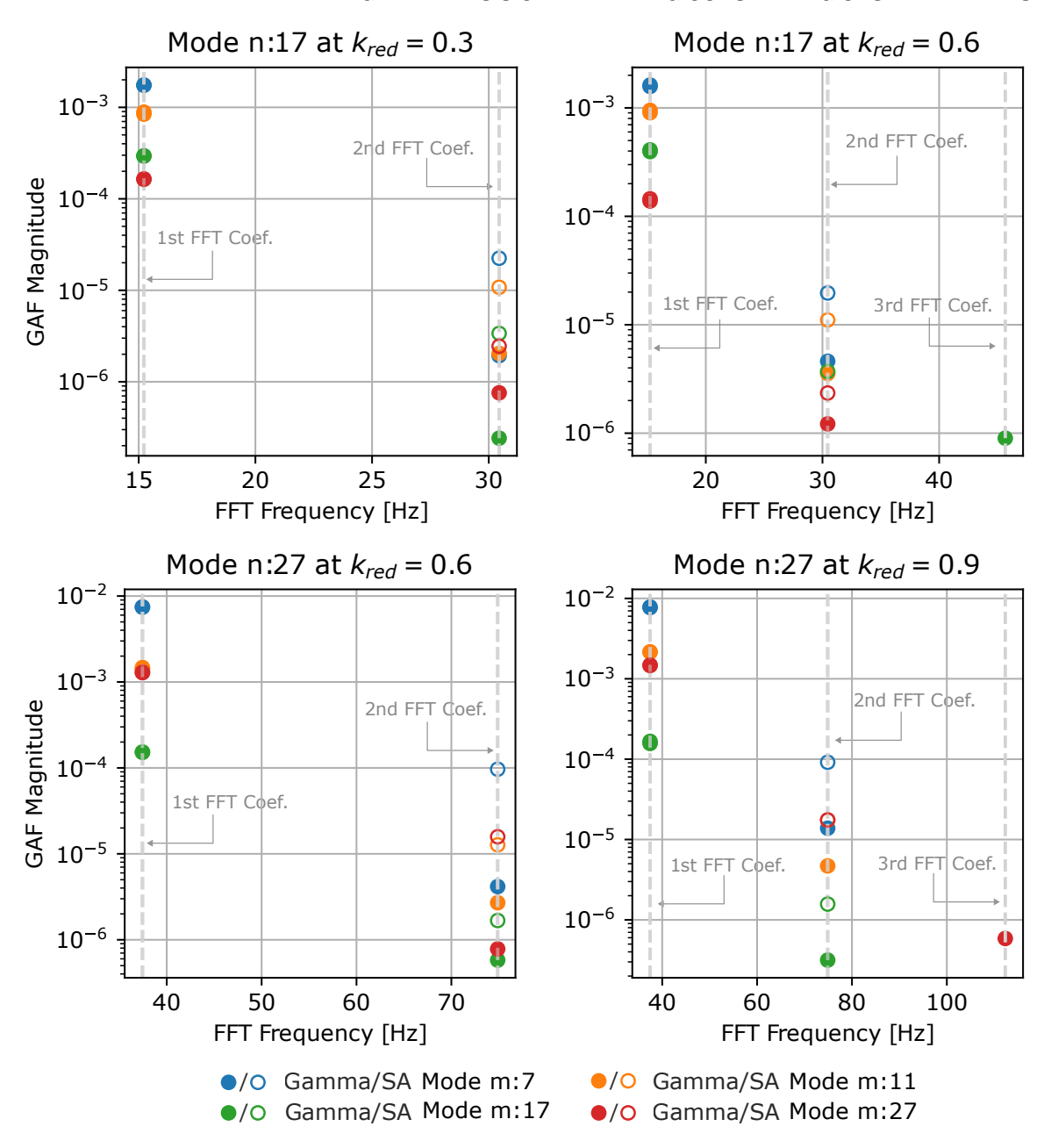


Figure 8 – Magnitude of the GAF entries in the frequency-domain over frequency- continuation of figure 7.

Both models exhibit a dominant first Fourier coefficient at the input frequency f_0 of mode n. The GAF magnitudes at f_0 are similar for both models, with an average deviation of 1.35% between them. On average, the SA model predicts higher magnitudes than the Gamma model. The largest deviation can be found for GAF 11-11 at $k_{red}=0.3$, where SA predicts a magnitude 14.3% higher than the Gamma model.

The GAF entries at higher Fourier coefficients have magnitudes that are significantly lower than the ones of the first coefficient. To be noted is, that there is no relevant frequency content at non-multiples of f_0 , indicating that the response predominantly contains harmonics of f_0 . While the SA model consistently identifies the second harmonic as the second most dominant coefficient, the Gamma model predicts that higher harmonics may have a greater impact than the second one. Overall, SA model tends to predict higher harmonics with higher magnitudes than the Gamma model.

Due to the difference in magnitude between the first harmonic and the higher frequency content of the GAF entries, the order of the model is reduced and only the first harmonic of the GAFs is accounted for in the subsequent analysis.

Figure 9 presents the phase shift in degrees for each GAF component as predicted with the SA and

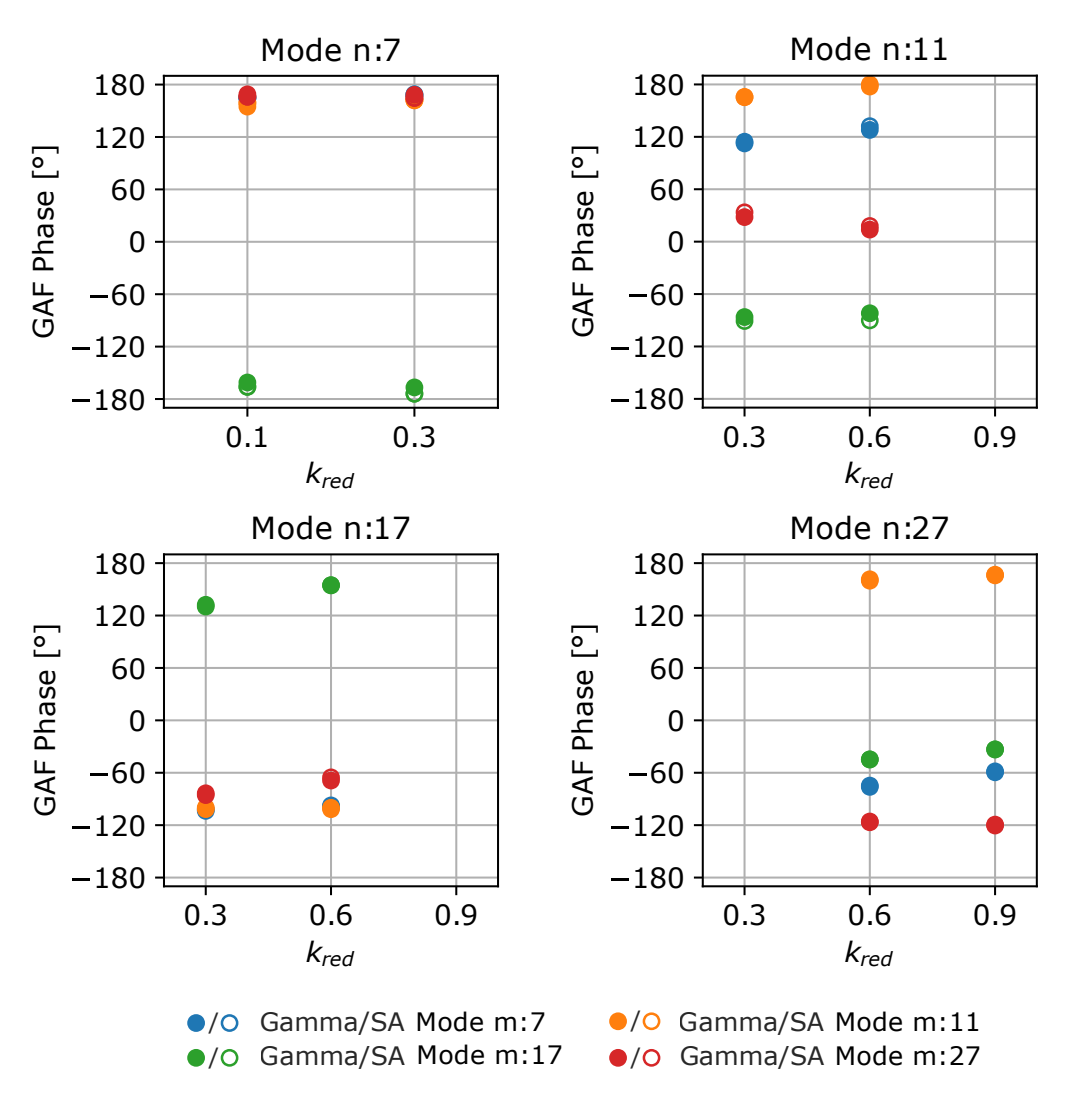


Figure 9 – Phase shift of the GAF matrix entries over k_{red} at $\alpha = 0^{\circ}$.

the Gamma model. The difference in phase between the two turbulence models is neglectable and for almost every case the two markers in figure 9 lie over each other. The average difference is approximately 0.15° and SA predicts a higher phase shift than Gamma. In general the phase shift increases with increasing k_{red} for $k_{red} > 0.3$.

4.4 Impact of Viscous Effects on the Generalized Aerodynamic Forces

To be noticed is that the free-stream reference angle of attack is $\alpha=2^\circ$. At this angle of attack, transition on the pressure side is forced by the turbulator for all investigated Re-numbers in steady-state conditions. However, to assess the impact of transition and viscous effects, one has to account for the change in effective angle of attack due to the structural oscillation. For the S1 bending mode the angle of attack can change as much as $\Delta\alpha=0.54^\circ$ for $k_{red}=0.6$. However, this $\Delta\alpha$ is not enough to significantly shift transition towards the LE at $\alpha=2^\circ$. Under the investigated conditions the transition on the pressure side is relatively insensitive to structural deformations with the selected amplitude. For this reason, the impact of viscous effects on the aerodynamic response may be damped. These boundary conditions were chosen based on steady state conditions to mitigate non-linearities arising from the boundary conditions, e.g. a distinct transition motion, and remain in the linear region customary of flutter analysis.

A more significant impact is expected if the angle of attack is reduced to match the lower corner of the laminar drag bucket, as a small reduction in effective angle of attack can drastically shift transition towards the leading edge [8]. A small amplitude structural deformations would suffice to induce such a displacement of the transition's location, which itself would induce viscous effects that alter the

aerodynamic response by means of a viscous cambering or decambering effect [8, 13].

To study these effects the S1 mode at $k_{red} = 0.1$ at an angle of attack of $\alpha = 0^{\circ}$ is simulated additionally. Figure 10 shows the corresponding Lissajous figures, which exhibit an elliptical shape.

Due to the smaller angle of attack, the non-zero frequency components of the GAF entries have shifted to lower values compared to the GAFs at $\alpha=2^{\circ}$. However, the vertical shift between the two turbulence models has increased compared to the previous cases at $\alpha=2^{\circ}$. At $\alpha=0^{\circ}$ and Re=2e6, transition on the pressure side has shifted upstream to approximately x/c=0.35. Due to the upstream shift of the transition's mean position, the turbulent boundary layer length increases. This results in a thickening of the boundary layer towards the trailing edge and a downwards deflection of the effective camber line, that acts as a positive flap deflection and is reflected in a higher DC component [13].

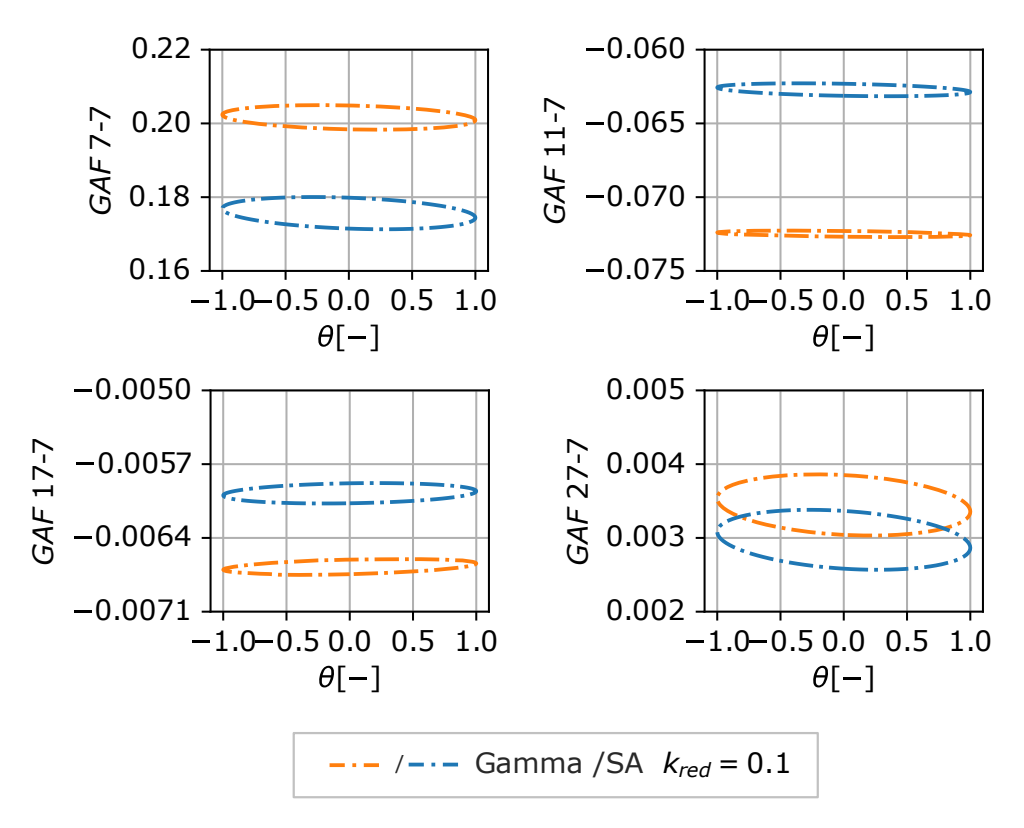


Figure 10 – Lissajous figures of generalized aerodynamic forces GAF_{mn} with n= 7, 11, 17 and 27 over the normalized structural deflection at $\alpha = 0^{\circ}$.

Regarding the non DC-components, SA shows a neglectable deviation in their magnitude and phase between the two angles of attack. In contrast to the previous case, the GAF curves predicted by the Gamma model exhibit a noticeable smaller semi-minor axis than the ones predicted with the SA model. This difference in the higher frequency content of the GAF is depicted in figure 11.

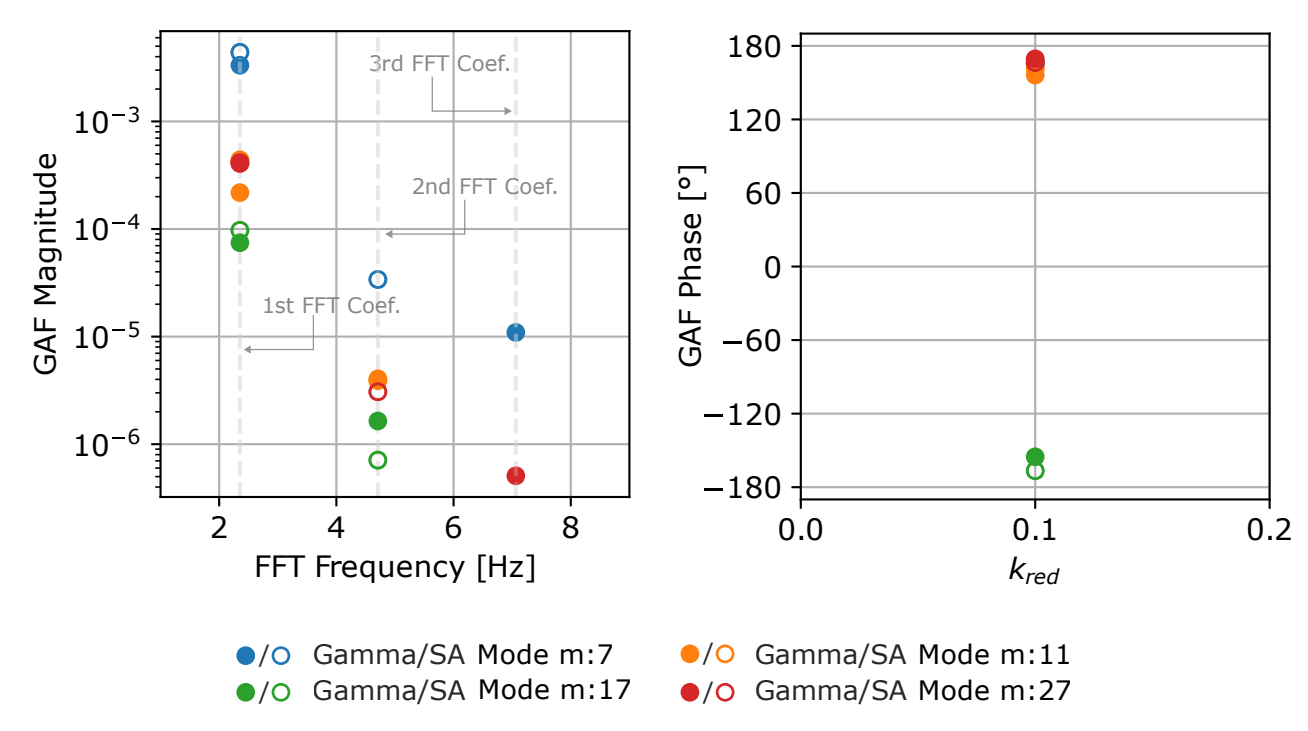


Figure 11 – Lissajous figures of generalized aerodynamic forces GAF_{m7} at $k_{red}=0.1$ and $\alpha=0^{\circ}$.

This behavior of the aerodynamic response is caused by viscous effects, that become more relevant under the new set of boundary conditions. Transition is more sensitive towards external factors and a changing effective angle of attack may induce an oscillation of the unsteady transition's location. The extent of this influence depends on the magnitude of the structural deformation. The higher the magnitude of the eigenvectors, the higher the amplitude of the transition's oscillation, which results in more relevant viscous effects.

A decreasing running length of the laminar boundary layer on the pressure side, i.e. an increasing running length of the turbulent boundary layer, causes an increase in the boundary layer thickness towards the TE. As already presented before, this causes a viscous cambering effect that acts as an effective positive viscous flap deflection during an upward motion of the the wing, counteracting the reduction in effective angle of attack and reducing the damping effect of the aerodynamic response. As a result the semi-minor axis decreases compared to the case at which the transition is forced by the turbulator during an entire oscillation period. The opposite occurs when the laminar boundary layer shifts downstream during the downward motion of the wing.

The difference in phase shift is neglectable except for GAF 17-7, where the SA model predicts a lower phase compared to the Gamma Model. The difference in phase shift is slightly higher than at $\alpha = 2^{\circ}$.

4.5 Aerodynamic Damping and Aerodynamic Stiffness

The GAF entries are further divided into their real and imaginary component to analyze the aerodynamic damping and stiffness, see section 2. The real and imaginary GAF components are shown in figure 12 for the simulated k_{red} at $\alpha=2^{\circ}$.

Both models predict similar trends in aerodynamic damping and stiffness over k_{red} . Real and imaginary components are similar in all cases. The aerodynamic forces generalized with mode 7 show the most noticeable deviations. GAF 7-11 and GAF 11-11 predicted by SA show a more significant decay in aerodynamic damping compared to the Gamma model with increasing k_{red} . For these cases, the Gamma model shows lower aerodynamic stiffness with increasing k_{red} . GAF 7-17 shows a similar behavior. On average, SA predicts a 7% higher aerodynamic stiffness and 2% higher aerodynamic damping than the transition model.

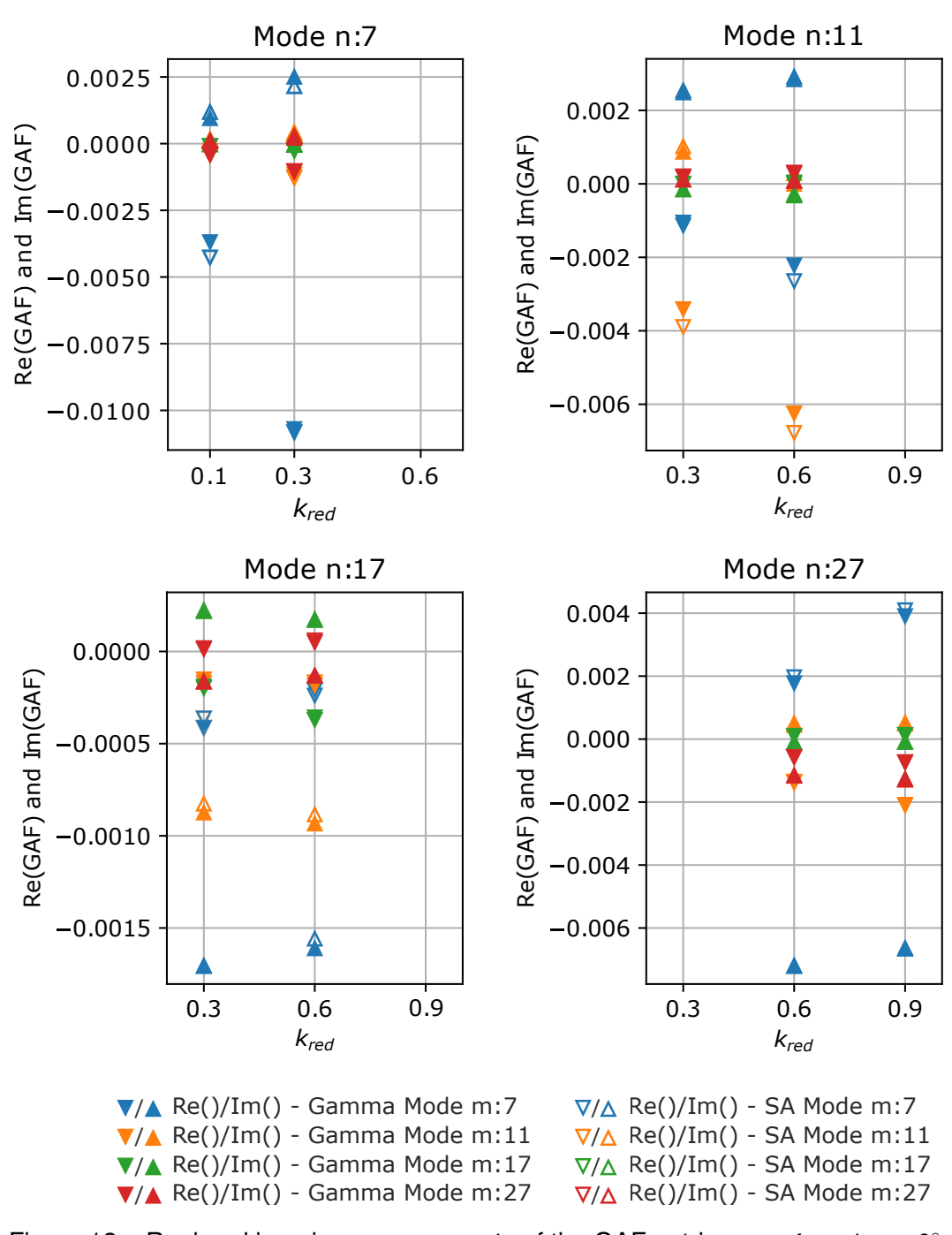


Figure 12 – Real and imaginary components of the GAF entries over k_{red} at $\alpha = 2^{\circ}$.

At $\alpha=0^\circ$ the real and imaginary components of the GAF predicted by the SA model do not present a visible change compared to the results at $\alpha=2^\circ$, see figure 13. However, the Gamma model predicts values closer to 0, indicating less aerodynamic stiffness and less aerodynamic damping.

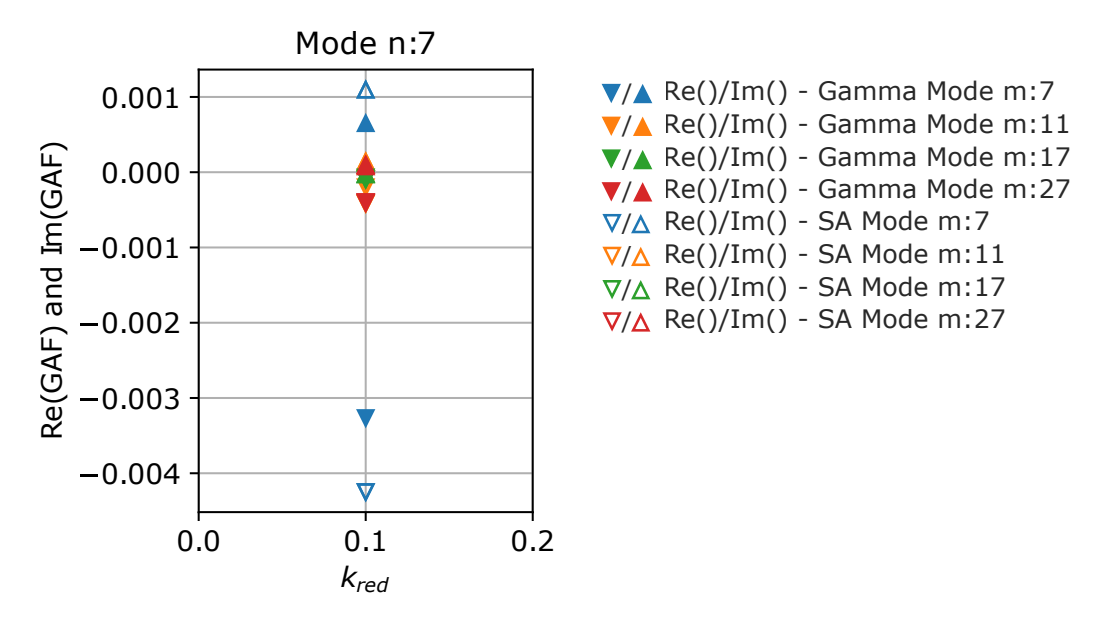


Figure 13 – Real and imaginary components of the GAF m-7 entries at $k_{red}=0.1$ and $\alpha=0^{\circ}$.

5. Conclusion and Outlook

This study presents a coupled Finite Element (FE) beam model of a sailplane with a Computational Fluid Dynamics (CFD) model to calculate the Generalized Aerodynamic Forces (GAF). The numerical investigation focuses on the impact of transition on the unsteady aerodynamic response of a modern sailplane's Natural Laminar Flow (NLF) wing, utilizing the Gamma-Transition Model. The GAF results are compared with those obtained using the fully turbulent Spalart-Allmaras (SA) model.

All simulations were performed at mean sea level conditions.

At an angle of attack $\alpha=2^\circ$, both models predict similar unsteady aerodynamic responses with the biggest deviations being in the DC component of the GAF entries. The aerodynamic response is clearly dominated by the frequency content at the input frequency of the structural deformation. The magnitude of the GAF entries at frequencies multiples of the input frequency are orders of magnitude lower than the first harmonic.

The GAF entries' first harmonics show similar magnitudes and phase shifts. On average, the SA model predicts 1.35% higher magnitudes and 2.5% higher phase shifts than the transition model.

The aerodynamic damping and stiffness predicted by the SA model and the Gamma-Transition model are similar. However, accounting for transition delivered less aerodynamic damping over k_{red} due to viscous effects. The relevance of these viscous effects is directly correlated with the chosen boundary conditions.

In future steps, a broader range of reduced frequencies can be included to gain deeper insights into the trends of aerodynamic damping and stiffness as functions of the reduced frequency.

6. Contact Author Email Address

To contact the author, please use the following email address: carlos.sebastia@tum.de

7. Acknowledgements

Support is provided in the framework ProFla (Prozesskette Flattern), funded by the German Federal Ministry for Economic Affairs and Climate Action under the grant of the German Federal Aviation Research Program (Luftfahrtforschungsprogramm, LuFo).

8. Copyright Statement

The authors confirm that they, and/or their company or organization, hold copyright on all of the original material included in this paper. The authors also confirm that they have obtained permission, from the copyright holder of any third party material included in this paper, to publish it as part of their paper. The authors confirm that they give permission, or have obtained permission from the copyright holder of this paper, for the publication and distribution of this paper as part of the ICAS proceedings or as individual off-prints from the proceedings.

References

- [1] Bisplinghoff R L, Ashley H, and Halfman R L. Aeroelasticity, Dover Publications, 1996.
- [2] Förster M. Aeroelastische Stabilitäts- und Antwortanalyse auf Basis Numerischer Strömungssimulation, *PhD thesis*, TU München, 2016.
- [3] Menter F R, Smirnov P E, Liu T, and Avancha R. A One-Equation Local Correlation-Based Transition Model, *Flow, Turbulence and Combustion*, Vol. 95, No. 4, pp. 583–619, 2015.
- [4] Rodden W P, and Albano E. A Doublet-Lattice Method for Calculating Lift Distributions on oscillating Surfaces in subsonic Flows, *AIAA Journal*, Vol. 7, No. 2, pp. 279–285, 1969.
- [5] Rozov V, Hermanutz A, Breitsamter C, and Hornung M. Aeroelastic Analysis of a Flutter Demonstrator With a Very Flexible High-Aspect-Ratio Swept Wing, *IFASD*,173,2017.
- [6] Winter M, Breitsamter C. Reduced-Order Modeling of Unsteady Aerodynamic Loads Using Radial Basis Function Neural Networks, *Deutscher Luft- und Raumfahrtkongress*, 2014.
- [7] Winter M. Nonlinear Aerodynamic Reduced-Order Modeling Using Neuro-Fuzzy Approaches, *PhD the-sis*.2021.
- [8] Sebastia C, and Hornung M, Numerical Analysis of Aerodynamic Flap Hinge Moment under Unsteady Flow Conditions considering Laminar-Turbulent Transition, *AIAA AVIATION Forum and Exposition*, 2023.
- [9] Simcenter STAR-CCM+ Documentation Version 2021.3, Siemens Digital Industries Software.
- [10] Thelen A, Leiffson L, and Beran P. Multifidelity Flutter Prediction Using Local Corrections to the Generalized AIC, *Aerospace Science and Technology*, 106(106032),2020.
- [11] O. O. Bendiksen, Review of Unsteady Transonic Aerodynamics: Theory and Applications, *Progress in Aerospace Sciences*, Vol. 47 (2), pp. 135–167, 2011.
- [12] Palacios R, Climent H, Karlsson A, and Winzell B. Assessment of Strategies for Correcting Linear Unsteady Aerodynamics Using CFD or Test Results, *IFASD*,074, 2001.
- [13] Drela, M. Flight Vehicle Aerodynamics, The MIT Press, 2014.
- [14] Colonia S, Leble V, Steijl R, and Barakos G. Assessment and Calibration of the Gamma-Equation Transition Model at Low Mach, *AIAA Journal*, Vol. 55, No. 4, 2017.